Research in Astronomy and Astrophysics, 22:085017 (12pp), 2022 August https://doi.org/10.1088/1674-4527/ac784e

The Distribution of UV Radiation Field in the Molecular Clouds of Gould Belt

Jifeng Xia (夏季风)[1,2,3], Ningyu Tang[4], Qijun Zhi[1,5], Sihan Jiao[2,3], Jinjin Xie[6], Gary A. Fuller[7,8], Paul F. Goldsmith[9], and Di Li[2,3]
[1] School of Physics and Electronic Science, Guizhou Normal University, Guiyang 550025, China; qjzhi@gznu.edu.cn
[2] National Astronomical Observatories, Chinese Academy of Sciences, Beijing 100101, China; dili@nao.cas.cn
[3] University of Chinese Academy of Sciences, Beijing 100049, China
[4] Department of Physics, Anhui Normal University, Wuhu 241002, China; nytang@ahnu.edu.cn
[5] Guizhou Provincial Key Laboratory of Radio Astronomy and Data Processing, Guizhou Normal University, Guiyang 550001, China
[6] Shanghai Astronomical Observatory, CAS, Shanghai 200030, China
[7] Jodrell Bank Centre for Astrophysics, Department of Physics & Astronomy, The University of Manchester, Manchester M13 9PL, United Kingdom
[8] I. Physikalisches Institut, University of Cologne, Zülpicher Str. 77, D-50937 Köln, Germany
[9] Jet Propulsion Laboratory, California Institute of Technology, 4800 Oak Grove Drive, Pasadena, CA 91109, United States of America
Received 2022 April 21; revised 2022 May 24; accepted 2022 May 30; published 2022 July 22

Abstract

The distribution of ultraviolet (UV) radiation field provides critical constraints on the physical environments of molecular clouds. Within 1 kpc of our solar system and fostering protostars of different masses, the giant molecular clouds in the Gould Belt present an excellent opportunity to resolve the UV field structure in star-forming regions. We performed spectral energy distribution (SED) fitting of the archival data from the Herschel Gould Belt Survey (HGBS). Dust radiative transfer analysis with the DUSTY code was applied to 23 regions in 14 molecular complexes of the Gould Belt, resulting in the spatial distribution of the radiation field in these regions. For 10 of 15 regions with independent measurements of star formation rate, their star formation rate and UV radiation intensity largely conform to a linear correlation found in previous studies.

Key words: ISM: clouds – (ISM:) dust – extinction – radiative transfer

1. Introduction

The interstellar medium (ISM) is the cradle of star formation. Its evolution is strongly affected by ultraviolet (UV) radiation. By ejecting electrons from dust grains and directly exciting atoms and molecules, UV photons ionize atoms, dissociate molecules and heat gases (e.g., Tielens & Hollenbach 1985; Ferrière 2001; Draine 2011). Kennicutt (1998) found a tight correlation between UV radiation and the star formation rate (SFR) in galaxies. In Galactic studies, most previous investigations focused on the distribution of the UV radiation field of individual nearby regions (e.g., Liseau et al. 1999; Pineda et al. 2010).

Within 1 kpc of our solar system, the Gould Belt containing a lot of molecular complexes provides an excellent opportunity to investigate the relationship between UV intensity and SFR under diverse environments (Ward-Thompson et al. 2007). Most molecular complexes of the Gould Belt harbor bright young OB stellar clusters or star-forming regions while the rest show little sign of star formation. For instance, the Orion complex is a widely studied giant molecular region with abundant clustering of OB stars and turbulent massive star formation (e.g., Lada et al. 1991; Tatematsu et al. 1998). Similar to Orion, the Serpens/Aquila Rift is a rich complex with well-known massive star-forming regions, e.g., the W40 HII region that contains embedded young high-mass stars (e.g., Kawamura et al. 1999). Although the Cepheus region contains an OB star (HD 200775 in Cep 1172), it has been generally considered as a low to intermediate mass star-forming region. The Lupus dark-cloud complex was found to be surrounded by about 70 T Tauri stars, with no indication of a massive OB star inside (e.g., Hara et al. 1999). The Chamaeleon-Musca dark-cloud complex, including Cha I, II, III and the Musca dark lane, is a region with low-mass star formation (e.g., Cambrésy 1999; Mizuno et al. 2001). IC 5146 is a filamentary dark cloud with scattered low star formation activity (e.g., Dobashi et al. 1994). The Pipe Nebula has been a primary example with little signs of disturbance from star formation (e.g., Onishi et al. 1999). No star formation was found in the Polaris Flare, a high-latitude translucent cloud (e.g., Heithausen & Thaddeus 1990).

Utilizing the Spectral and Photometric Imaging Receiver (SPIRE) and Photodetector Array Camera and Spectrometer (PACS) instruments on board the Herschel[10] Space Observatory, the Herschel Gould Belt Survey (HGBS) covered a substantial fraction of the Gould Belt. Specifically, images were taken at 250, 350 and 500 μm for regions with $A_V >$ 3 mag with SPIRE and at 70 and 160 μm for those with $A_V >$ 6 mag with PACS. This survey covers the following 14

[10] Herschel is a European Space Agency (ESA) space observatory with science instruments provided by European-led Principal Investigator consortia and with important participation from NASA.

molecular complexes: Aquila, Cepheus, Chamaeleon, Corona Australis, IC 5146, Lupus, Musca, ρ Oph, Orion, Perseus, Pipe Nebula, Polaris, Taurus and Serpens.

The dust radiative transfer model, DUSTY (Ivezic & Elitzur 1997; Nenkova et al. 2000) accommodates different kinds of geometry and radiation parameters. Li et al. (2003) demonstrated the utilities of the DUSTY code to derive the UV intensity of the Orion clouds based on fitting the dust temperature data. We further develop the recipe and apply it to the full set of HGBS data.

This paper is organized as follows. In Section 2, we introduce information on column density, dust temperature and SFR toward the HGBS molecular complexes. The DUSTY radiative transfer code and method for calculating the UV radiation intensity map are described in Section 3. Results and further discussions are presented in Sections 4 and 5, respectively. The summary is in Section 6.

2. Data

2.1. Herschel Dust Continuum Emission

Dust emission is almost always optically thin at (sub)millimeter wavelengths and can thus act as a surrogate tracer of the total (gas + dust) mass along the line of sight (LOS) (Roy et al. 2014). The HGBS took a census of the nearby (0.5 kpc) molecular cloud complexes for an extensive imaging survey of the densest portions of the Gould Belt, down to a 5σ column sensitivity $N_{\rm H_2}$ $\sim 10^{21}$ cm^{-2} or A_V $\sim$1 mag (André et al. 2010). We use the HGBS data to generate the column density map of 23 molecular clouds that belong to 14 molecular complexes of the Gould Belt. The molecular clouds studied in this paper are Aquila M2 (André et al. 2010), Cep 1151, Cep 1172, Cep 1228, Cep 1241, Cep 1251 (Di Francesco et al. 2020), Cham I, Cham II, Cham III (Winston et al. 2012), (Alves de Oliveira et al. 2014), CraNS (Bresnahan et al. 2018), IC 5146 (Arzoumanian et al. 2019), Lup I, Lup III, Lup IV (Rygl et al. 2013), Musca (Cox et al. 2016), ρ Oph (Roy et al. 2014), Orion B (Könyves et al. 2020), Orion A (S. Jiao et al. 2022, in preparation), Perseus (Pezzuto et al. 2012), Pipe (Peretto et al. 2012), Polaris (André et al. 2010), Taurus (Arzoumanian et al. 2019) and Serpens (Fiorellino et al. 2021).

2.2. Deriving Dust Temperature and Column Density Based on SED Fitting

The dust temperature and column density map toward 22 of 23 regions were downloaded from the HGBS Archive.[11] We obtained dust distribution and improved the image quality of the Orion A region, based on a novel image combination technique (S. Jiao et al. 2022, in preparation).[12] The procedure to derive the dust temperature and dust/gas column density images of Orion A is similar to that in Roy et al. (2014). Before performing any spectral energy distribution (SED) fitting, all images at multiple bands were convolved into a beam size of $36\farcs3$ at 500 μm. We weighted the data points by the measured noise level in the least-squares fits. We adopted the dust opacity per unit mass at 300 μm of 0.1 cm^2 g^{-2} (Hildebrand 1983), and assumed a gas-to-dust mass ratio of 100. As a modified blackbody assumption, the flux density S_ν at a certain observing frequency ν is given by

$$S_\nu = \Omega_m B_\nu(T_d)(1 - e^{-\tau_\nu}), \quad (1)$$

where $B_\nu(T_d)$ is the Planck function at temperature T_d and Ω_m is the beam size. The total column density N of gas and dust can be approximated by

$$N = \frac{\tau_\nu}{\kappa_\nu \mu {\rm m}_H}, \quad (2)$$

where the dust opacity $\kappa_\lambda = \kappa_{300\mu{\rm m}}(\lambda/300\ \mu{\rm m})^\beta$ (β was fixed to a constant value of 1.8), $\mu = 2.8$ is the mean molecular weight and m_H is the mass of a hydrogen atom. The graybody dust temperature (T_d) thus calculated has ignored the dependence of dust temperature on grain size (Li et al. 1999), but has been shown to be within a couple of kelvins of the gas temperatures in well coupled regions (Goldsmith 2001; Li et al. 2013; Wang et al. 2020; Xie et al. 2021). The effect of scattering opacity (e.g., Liu 2019) can be safely ignored in the case focusing on >0.05 pc scale structures.

2.3. Star Formation Rates

The SFRs were determined through SFR $= N({\rm YSO})\langle M\rangle \tau^{-1}$, in which N(YSO) is the YSO number in the molecular region, $\langle M\rangle$ is the mean mass of stars and τ is the relevant evolution timescale.

The identification of YSOs requires careful discrimination against background stars and galaxies. Star-forming galaxies were the most problematic source of contaminants. A combination of color–color and color–magnitude diagrams of both Spitzer and 2MASS data was adopted to reject contaminants. The detailed descriptions of this process are provided in Evans et al. (2009). Dunham et al. (2013) provide a YSO catalog for Gould Belt clouds. To convert number of YSOs to mass of forming stars, Evans et al. (2014) adopted mean mass of stars $M_\star = 0.5\ M_\odot$, based on a fully sampled initial mass function (IMF) (Kroupa 2002). The relevant timescales were derived by classifying YSOs into standard SED classes based on 2 to 24 μm data.

Table 1 lists the SFRs (Lada et al. 2010; Evans et al. 2014) we adopted in this paper.

[11] The website of HGBS Archive: http://www.herschel.fr/cea/gouldbelt/en/index.php.

[12] The column density and dust temperature of Orion A were not published on the website of HGBS archive by 2022.

Table 1
Star Formation Rate of 15 Molecular Regions

Cloud Name	R.A. (deg)	Decl. (deg)	Distance[a] (pc)	SFR[a] (10^{-6} $M_\odot$ yr^{-1})	Category[b]
Orion A	84.52	−7.03	423	715	I
Orion B	86.90	0.10	423	159	I
Serpens	278.78	4.6E-06	429	56	I
Perseus	53.92	31.53	250	150	I
ρ Oph	246.87	−24.21	125	79	I
Musca	186.81	−71.54	200	3	I
Lupus III	242.51	−39.08	200	17	II
Lupus IV	241.15	−42.07	150	3	II
Aquila	277.43	−2.78	260	322	II
IC 5146	327.19	47.49	460	24	II
Cham I	165.46	−77.40	150	20.5	II
Cham II	195.23	−77.41	178	6	II
Cham III	190.47	−79.82	150	1	II
Pipe	260.78	−26.40	145	5	II
Taurus	65.08	27.72	153	84	II

Notes. The coordinates are determined by the data of HGBS.
[a] The values of distances and SFRs are obtained from Lada et al. (2010) and Evans et al. (2014).
[b] A region with both OB stars and YSOs is defined as Category I; a region with YSOs only is defined as Category II.

3. Method

3.1. The DUSTY Code

The public DUSTY code (Ivezic & Elitzur 1997) solves the radiative transfer problems through a fully scale-free method. By adopting this scaling method, the DUSTY code solves the spherically symmetric (1-D) problem with a single central radiation source and surrounding spherically symmetric dusty envelope, in which the radial dust density profile is arbitrary. In addition, a dusty plane-parallel slab with illumination from one or both sides at an arbitrary angle is also available.

This code utilizes the scaling properties to minimize the number of input parameters. Parameters describing the external radiation, dust and gas properties, and cloud geometry are needed for inputs. For the case of spherical geometry, they include number, spectral shape and flux of the external source, chemical composition of dust, the lower and upper limits of dust optical depth, and density distribution of dust. For the case of slab geometry, an extra selection of source side is needed.

Once the input parameters are chosen, the DUSTY code outputs the value of dust temperature as a function of gas optical depth.

3.2. Parameter Setting in DUSTY Code

We adopted the slab geometry for our calculations. The incident angle between UV radiation and the slab, θ, is treated as 0 degree, $\theta = 0°$, indicating perpendicular UV radiation toward the slab. The selected radiation wavelength of 0.365 μm is located in the central wavelength of the UV band. The dust sublimation temperature, which is the highest temperature at which the dust grains can exist, is chosen to be the common value of 1500 K. The value ranges of gas optical depth and dust temperature are chosen as [0,30] and [0, 50] K, respectively.

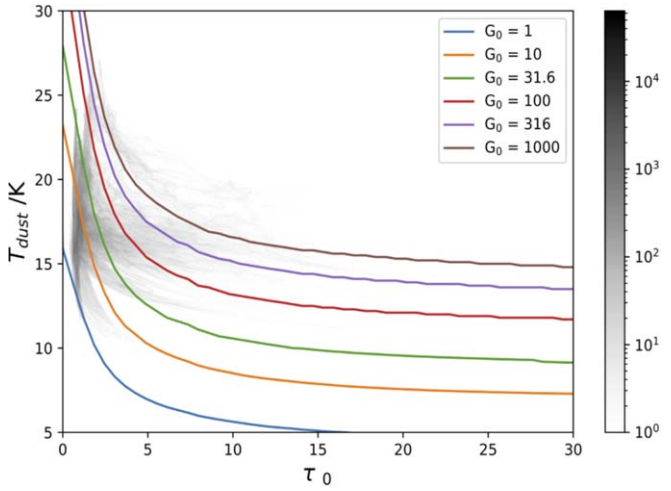

Figure 1. Relationship between dust temperature and optical depth. Results for the observed ρ Oph data are shown with gray points. Solid colored lines represent model calculations from the DUSTY code with different UV intensity values, G_0.

With the above selections, the UV radiation intensity, G_0 is the only parameter that determines the relationship between dust temperature and gas optical depth. As for the optional UV radiation flux received by one side of the slab, six sets of UV intensity ($G_0 = 1$, 10, 31.6, 100, 316, and 1000) compared to a standard Habing field (e.g., Hughes et al. 2017) of 1.6×10^{-6} W m^{-2} are introduced for calculation.

3.3. Distribution of UV Intensity Field

In order to produce the spatial distribution of UV radiation field of the Gould Belt, we combined the DUSTY model calculations and the HGBS data.

The derived H_2 column density and dust temperature map of HGBS molecular complexes with pixel size of 3″ were convolved and re-sampled with the beam size of 36.″3 at 500 μm. We are focusing on dense molecular regions, and the contribution from atomic hydrogen can be ignored. Thus the H_2 column density was converted into gas optical depth at V band through the following equation (Bohlin et al. 1978; Greenberg 1968; Rachford et al. 2009)

$$\tau_V = \frac{A_V}{1.086} = \frac{1.07 \times 10^{-21} N_{\rm H_2}}{1.086}. \quad (3)$$

As an example, the derived relationship between $T_{\rm dust}$ and gas optical depth (τ_V) of all pixels for the ρ Oph cloud can be found in Figure 1. We obtained the UV intensity of each pixel by interpolating the results from observations with those from

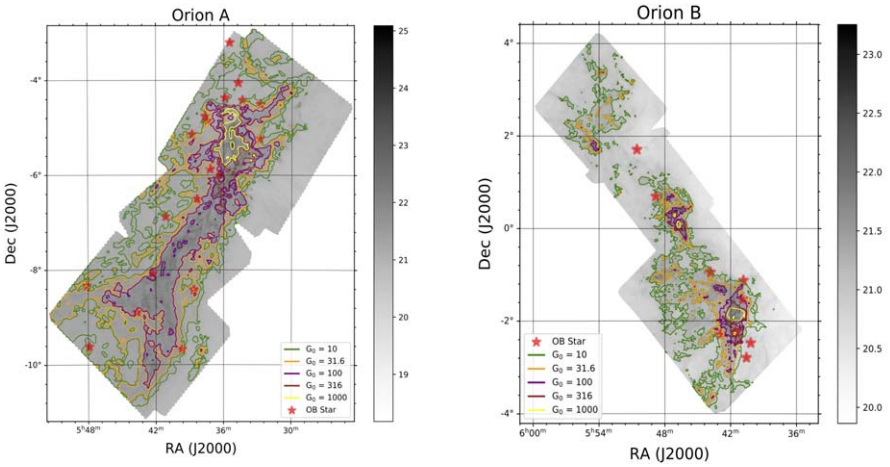

Figure 2. Contours of UV intensity overlaid on H_2 column density map of the Orion A (*left panel*) and Orion B (*right panel*) regions. The column density $N(H_2)$ is shown with $\log_{10} N(H_2)$ value. The red star implies the location of an OB star in this region.

DUSTY model calculations. The spatial distribution of the specific UV radiation field of each HGBS molecular complex can be derived.

4. Results

After applying the procedures described in Section 3, we obtained the UV intensity distribution of 23 regions in 14 molecular complexes of the Gould Belt.

4.1. Spatial Distribution of UV Intensity

As an example, we present the spatial distribution of selected UV intensity (G_0 = 1, 10, 31.6, 100, 316 and 1000) for three molecular complexes: Orion (Category I), Aquila (Category II) and Polaris (Category III). Descriptions of the other complexes are presented in Appendix.

4.1.1. Orion

The Orion molecular complex is the most active star-forming region within 500 pc (Megeath et al. 2012). Orion A and Orion B molecular clouds are covered by HGBS. Located in Orion A, the Orion Nebula cluster is a significant laboratory for understanding the IMF. The Orion B molecular cloud is one of the clouds scattered along the region named Orion-Eridanus superbubble, which was created by supernova explosions (Könyves et al. 2020). The Orion B cloud is ∼423 pc away and covers an area of $\sim 6.8 \times 8.6$ deg^2 (Evans et al. 2014). The total mass of these two molecular clouds exceeds 2×10^5 $M_\odot$ (Megeath et al. 2012).

As affirmed in Figure 2, the UV intensity of these two regions displays a tight correlation with the OB stars.

4.1.2. Aquila

The Aquila field is a very active star-forming region at a distance of about 260 pc (Evans et al. 2014). With size of ∼7.56 pc, the mass of this molecular complex is about 24 446 $M_\odot$, of which two-thirds is composed of dense cores (Evans et al. 2014). The existence of a dense cloud leads to the highest level of background cloud emission in HGBS. A cluster of YSOs but no OB stars was detected in this region. The number of YSOs in this region exceeds 1000.

As shown in Figure 3, the intensity of the radiation field distribution varies from $G_0 = 1$ to $G_0 = 1000$. We found a certain correlation between the spatial distribution of YSOs and UV radiation field. The possible reason responsible for this is discussed in Section 5.

4.1.3. Polaris

The Polaris Flare has a distance of about 352 pc and total mass of about 5500 $M_\odot$ (Zucker et al. 2019). It is a high-latitude translucent cloud with little or no obvious star formation activity. It is expected to have the lowest level of background cloud emission (Heithausen & Thaddeus 1990). Neither OB stars nor YSOs were detected in this region. As depicted in Figure 4, the UV intensity G_0 of almost the whole region is smaller than 10.

4.2. UV Intensity vs. N(H_2)

We present a statistical result between UV intensity G_0 and peak H_2 column density $N(H_2)$ of each molecular cloud in Figure 5. The correlation between G_0 and $N(H_2)$ can be fitted with a linear function of

$$\log(G_0) = (0.62 \pm 0.12)\log(N(H_2)) - (11.56 \pm 2.87), \quad (4)$$

for all complexes. It becomes

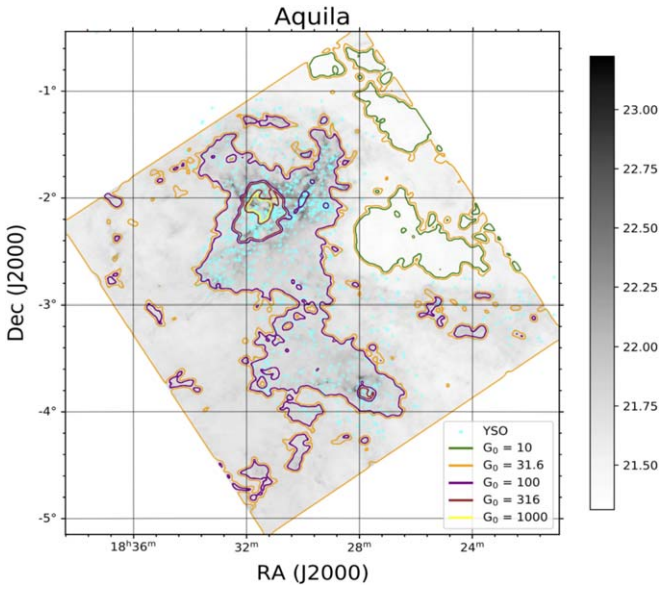

Figure 3. Contours of UV intensity overlaid on H_2 column density map of the Aquila molecular complex. The column density $N(H_2)$ is shown with $\log_{10} N(H_2)$ value. The cyan dots represent the locations of YSOs.

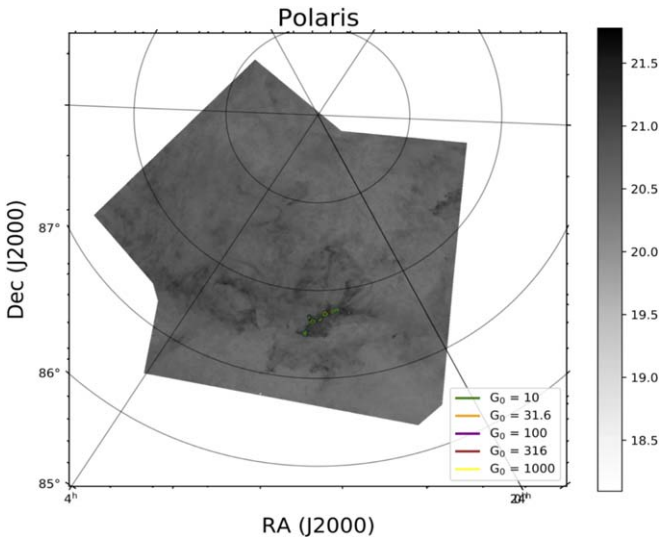

Figure 4. Contours of UV intensity overlaid on H_2 column density map of the Polaris region. The labels of the figure are the same as those in Figure 3. No YSOs or OB stars were found in this region.

$$\log(G_0) = (0.94 \pm 0.17)\log(N(H_2)) - (18.76 \pm 3.91), \quad (5)$$

when Orion A was not included.

5. Discussion

In this paper, we obtained the distribution of UV radiation field toward 23 regions of 14 molecular complexes in the Gould Belt through dust radiative analysis.

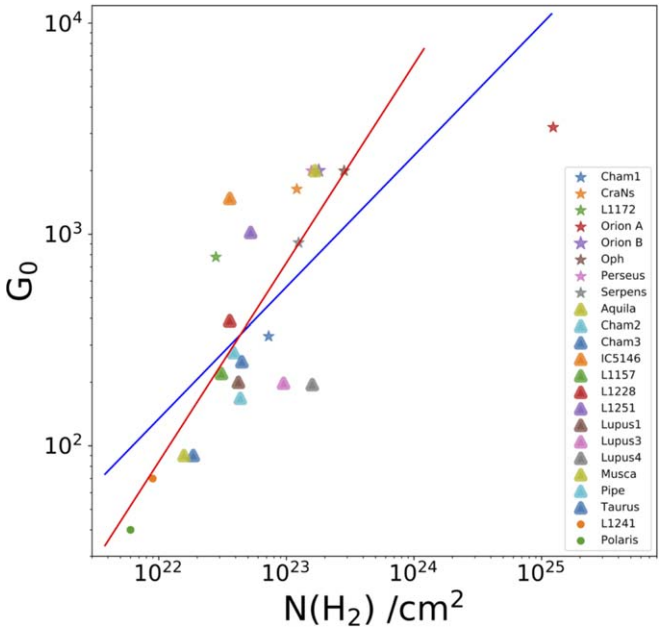

Figure 5. The relationship between UV intensity G_0 and peak H_2 column density $N(H_2)$. Filled stars, triangles and circles represent categories I, II and III, respectively. The blue solid line corresponds to a linear fit of all clouds. The red solid line signifies a linear fit when Orion A is excluded.

5.1. Uncertainty Analysis

The main assumption of such analysis is that the heating of dust was mainly due to UV radiation from massive stars. This has been demonstrated to be valid in the presence of massive stars, particularly OB clusters (e.g., Li et al. 1999, 2003). In more quiescent regions, however, dynamic feedback through outflows and bubbles from low-mass stars have proven to be capable of sustaining the turbulence in, e.g., Taurus (Li et al. 2015), which thus presumably may result in some dust heating. However, even supposing the gas and dust are closely coupled, there is no sign of elevated temperatures close to low-mass YSOs in Taurus (Goldsmith et al. 2008). We thus consider the heating of dust from low-mass YSOs to be minor.

In testing the model, we find that the incident angle more strongly affects absolute value of the derived UV field, rather than its distribution. To obtain robust results for the Gould belt sample in a systematic way, we set the incident angle to zero. Further investigation of the individual radiation geometry is warranted.

5.2. Compare with Star Formation Rate

We obtain the total UV fluxes in Aquila, Cham I, Cham II, Cham III, IC 5146, Lupus III, Lupus IV, Serpens, Musca, ρ Oph, Orion A, Orion B, Pipe, Perseus and Taurus by adding up the DUSTY outputs for each region and comparing them with the SFR in Lada et al. (2010), Evans et al. (2014).

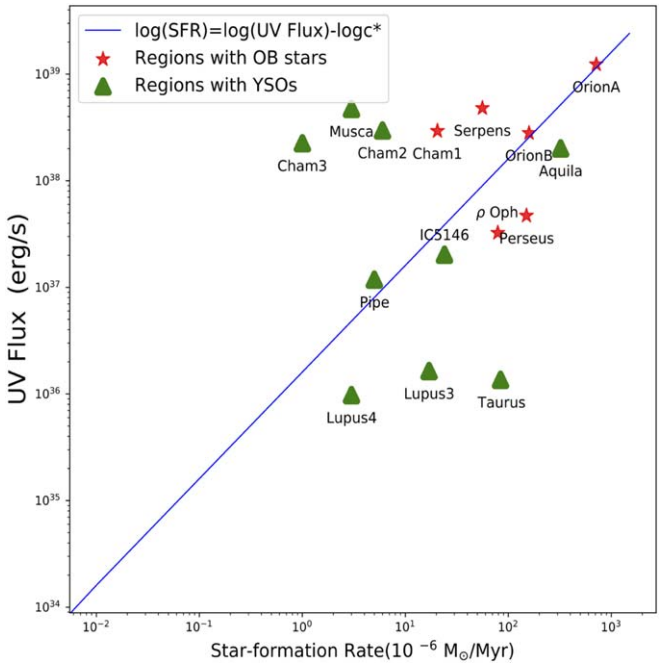

Figure 6. The relationship between total UV flux and SFR in 15 molecular clouds including Lupus, Corona Australis, Pipe, Musca, ρ Oph, Perseus, Aquila, Orion A, Orion B, Serpens, IC 5146 and Chamaeleon. The blue line indicates the formula in Equation (6). Regions with massive OB stars fit the blue line better than regions with YSOs.

UV emission is a direct tracer of the recent SFR since it traces the photospheric emission of young stars. The investigation of SFR of extragalaxies has been revolutionized with observations by the Galaxy Evolution Explorer (GALEX) telescope (Martin et al. 2005). By combining the UV data and IMF, the relationship between SFR and UV luminosity (Hao et al. 2011; Kennicutt & Evans 2012) can be described as

$$\log(\dot{M}_{\odot}) = \log(L_{\nu}) - \log(C), \quad (6)$$

where $\dot{M}_{\odot}$ is SFR in the unit of $10^{-6}\ M_{\odot}\ \mathrm{yr}^{-1}$, L_{ν}(FUV) is far ultraviolet (FUV) luminosity in the unit of erg s^{-1} and log $(C) = 43.35$ is a conversion constant.

The relationship between UV intensity and SFR for 15 molecular regions of the Gould Belt is presented in Figure 6. The blue line signifies the correlation between UV flux by OB stars and SFR. The correlation conforms to the general expectation. Regions with prominent OB clusters tend to be more consistent with the expectation. The scatter is bigger where there is no OB star. Different regions in the same molecular cloud tend to have similar UV fields, but different SFR. The less massive YSOs seem to have little effect on the UV distribution.

6. Summary

By interpreting dust continuum data through radiative transfer analysis, we obtained the UV intensity distribution toward 23 molecular regions in the Gould Belt. The main results of this study are summarized as follows,

1. The UV intensity G_0 of molecular clouds ranges from 1 to over 1000, relative to the Habing interstellar field.
2. The UV distribution in the majority of the molecular regions shows a tight correlation with that of OB stars and/or YSOs.
3. The UV intensity of 10 molecular regions conforms to an expected linear correlation with the SFR.

Acknowledgments

This work is supported by the National Natural Science Foundation of China (NSFC, Grant Nos. 11988101, 11725313, 11721303 and U1731238), the International Partnership Program of Chinese Academy of Sciences grant No. 114A11KYSB20160008, the National Key R&D Program of China No. 2016YFA0400702, Q.-J. Z. is supproted by the Guizhou Provincial Science and Technology Foundation (Nos. [2016]4008, [2017]5726-37,) and the Foundation of Guizhou Provincial Education Department (No. KY (2020) 003). This research was carried out in part at the Jet Propulsion Laboratory, California Institute of Technology, under contract with the National Aeronautics and Space Administration. This research made use of APLPY, an open-source plotting package for Python (Robitaille & Bressert 2012).

Appendix
UV Distribution of the Gould Belt Complexes

A.1. Cepheus

Located at a high decl., the Cepheus molecular complex includes many regions that have loose association with compact

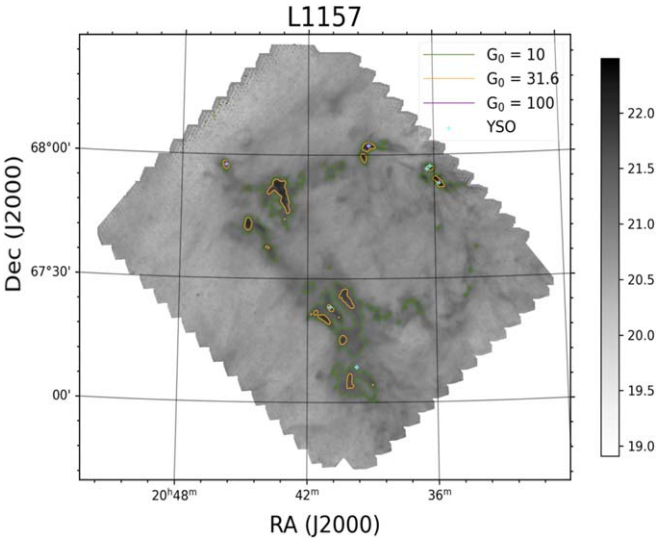

Figure A1. Contours of UV intensity overlaid on H_2 column density map of the L1157 region. The labels of the figure are the same as those in Figure 3.

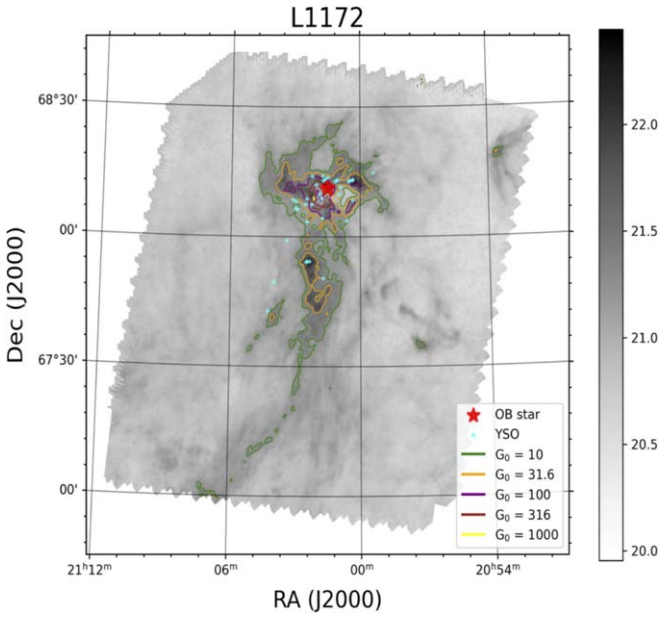

Figure A2. Contours of UV intensity overlaid on H_2 column density map of the L1172 region. The labels in the figure are the same as those in Figure 3. The red star implies the location of an OB star in this region.

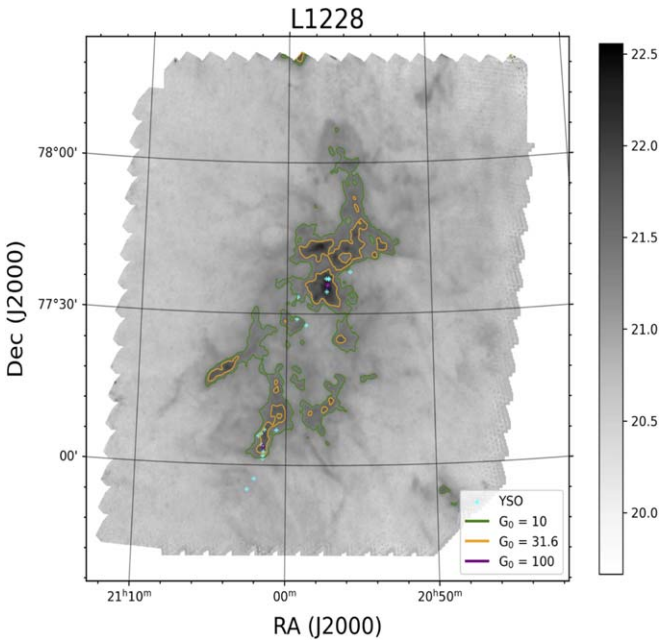

Figure A3. Contours of UV intensity overlaid on H_2 column density map of the L1228 region. The labels in the figure are the same as those in Figure 3.

dark clouds. HGBS contains five regions in the Cepheus molecular complex, Cep 1157 (Figure A1) (also known as L1157, the same below), Cep 1172 (Figure A2), Cep 1228 (Figure A3), Cep 1241 (Figure A4) and Cep 1251 (Figure A5). The distances of the five regions are considered to be 200–300 pc.

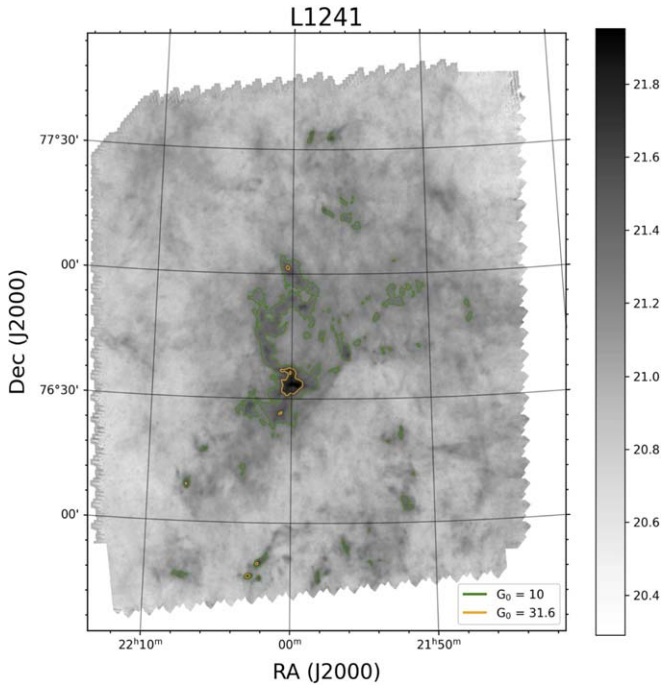

Figure A4. Contours of UV intensity overlaid on H_2 column density map of the L1241 region. The labels in the figure are the same as those in Figure 3. There are neither YSOs nor an OB star in this region.

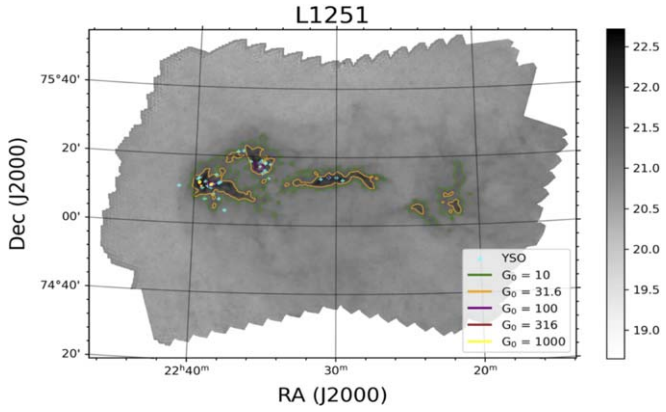

Figure A5. Contours of UV intensity overlaid on H_2 column density map of the L1251 region. The labels in the figure are the same as those in Figure 3.

The masses of L1157, L1172, L1228, L1241 and L1251 are 1400 $M_\odot$, 1900 $M_\odot$, 1600 $M_\odot$, 3200 $M_\odot$ and 1800 $M_\odot$ (Di Francesco et al. 2020). L1172 is the host of the bright NGC 7023 reflection nebula, which contains the bright B star HD 200775 in these five regions. L1241 and L1251 lie within the Cepheus Flare Shell. L1241 is the only one region without YSOs nor OB star. Some YSOs are found in L1251. The L1228 is located at the edge of the Cepheus Flare Shell, while L1157 and L1172 are located outside of the Cepheus Flare Shell.

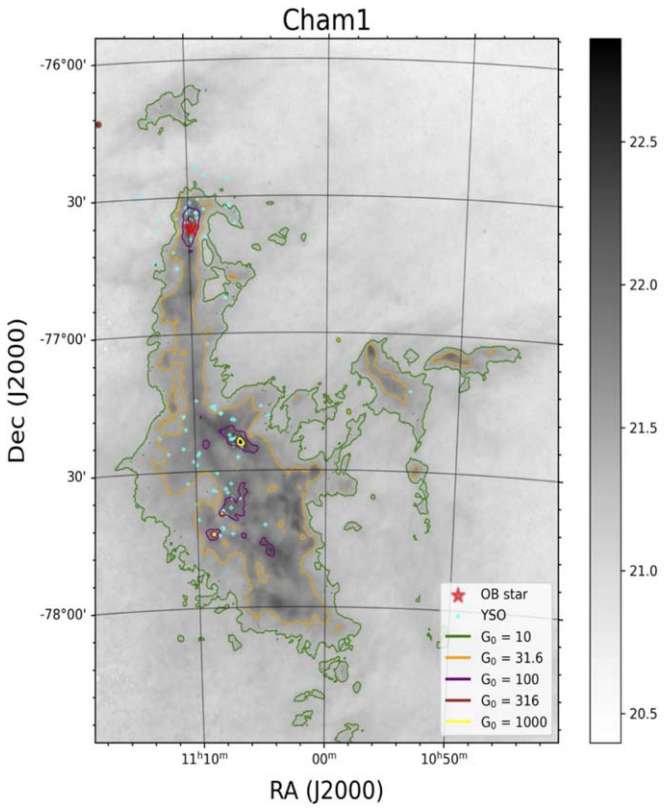

Figure A6. Contours of UV intensity overlaid on H_2 column density map of the Cham I region. The labels of the figure are the same as those in Figure A2.

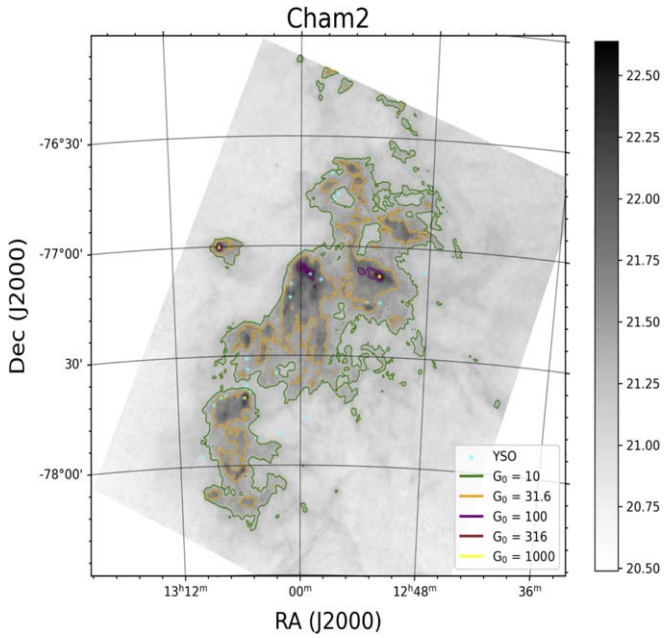

Figure A7. Contours of UV intensity overlaid on H_2 column density map of the Cham II region. The labels of the figure are the same as those in Figure 3.

The radiation field distribution of these five regions is quite different depending on the existence of massive stars and YSOs. As demonstrated in Figure A2, the UV intensity of L1172 around HD 200775 can exceed 1000 G_0. For the L1157 (Figure A1), L1228 (Figure A3) and L1251 (Figure A5) regions, obvious higher UV intensity can be found around the YSOs. The UV intensity in L1241 is smaller than 31.6 G_0 as there are neither massive stars nor YSOs in this region.

A.2. Chamaeleon

Chamaeleon is a nearby low-mass star-forming region containing Cham I, Cham II and Cham III. The distance from the regions in Chamaeleon is about 150 pc (Evans et al. 2014). The entire Cham I region covers an area about 5 deg^2, containing about 200 known low-mass YSOs, making it one of the closest and richest star-forming regions. The total mass of this cloud is about 482 $M_\odot$, one third of which is dense gas (Evans et al. 2014). Though there is abundant low-mass YSOs in Cham I, there is only one B star: HD 97300 in the northern part of the cloud (Winston et al. 2012).

The Cham II region contains a smaller number (∼60) of YSOs compared to the Cha I region. The size of Cham II is about 1.78 pc. The total mass of Cham II is about 637 $M_\odot$ while one-tenth is dense gas. As the largest cloud among the three regions with a total mass of 746 $M_\odot$, Cham III contains little dense gas and only a few YSOs (Alves de Oliveira et al. 2014).

Due to the differences in containing YSOs and dense gas, the UV intensity distributions of Cham I, Cham II and Cham III are expected to vary significantly. As shown in Figures A6, A7 and A8, the maximum UV intensity value decreases from Cham I to Cham III, which is proportional with the existence of OB stars.

A.3. CraNS

With distance of around 130 pc and being out of the Galactic plane, the CraNS (Corona Australis) molecular cloud is a low-mass star-forming region. The total mass of this region is about 279 $M_\odot$, half of which is dense gas (Evans et al. 2014). There is an OB star (V* R CrA) and a cluster of YSOs in this region (Bresnahan et al. 2018). As affirmed in Figure A9, the derived UV intensity G_0 around the OB star can exceed 1000.

A.4. IC 5146

With a distance of ∼460 pc, the IC 5146 region covers an area of $\sim 3.1 \times 2.5$ deg^2. The total mass of this cloud is about 3.7×10^3 $M_\odot$ (Arzoumanian et al. 2019). There is little dense gas and not an OB star in this region (Evans et al. 2014). Abundant YSOs exist in this region. We present UV intensity distribution for IC 5146 in Figure A10. The UV intensity G_0 can reach 31.6 around the YSOs.

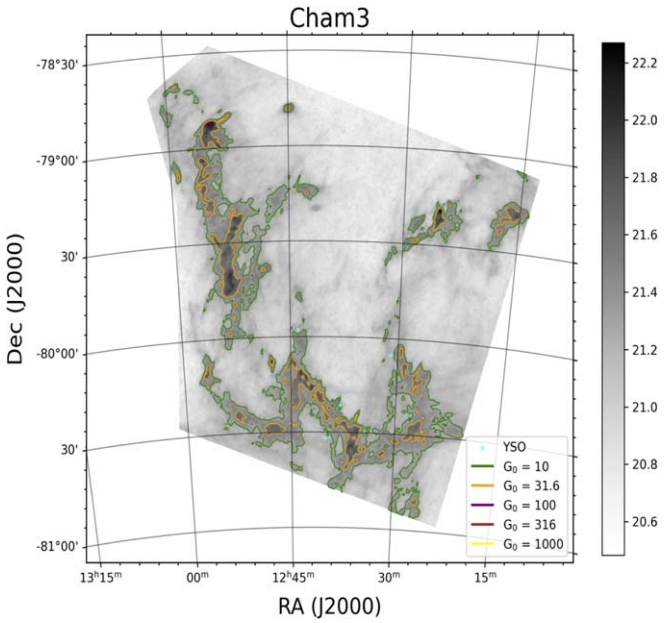

Figure A8. Contours of UV intensity overlaid on H_2 column density map of the Cham III region. The labels of the figure are the same as those in Figure 3.

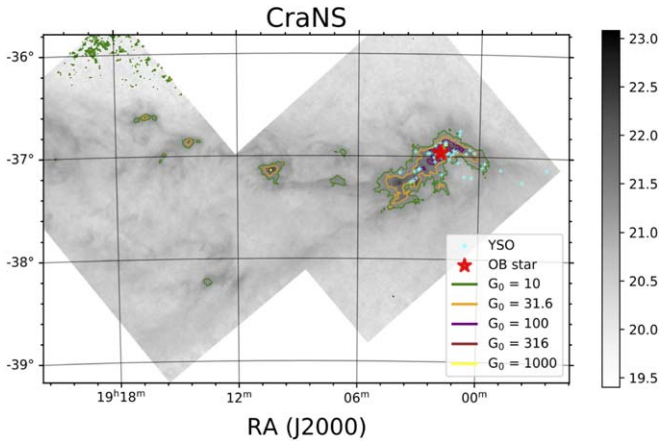

Figure A9. Contours of UV intensity overlaid on H_2 column density map of the CraNS region. The labels of the figure are the same as those in Figure 3.

A.5. Lupus

The distance of the Lupus molecular complex is about 189 pc (Zucker et al. 2019). The HGBS surveyed three clouds in this complex: the Lupus I, Lupus III and Lupus IV clouds. Among the three clouds, the Lupus I cloud is the youngest. The mass of Lupus I is about 512 $M_{\odot}$. Lup III is the most evolved cloud with a mass of ∼912 $M_{\odot}$. The Lupus IV cloud has a middle property between the Lupus I and III clouds. The mass of dense gas in the Lupus IV cloud is 50 $M_{\odot}$, accounting for about one quarter of the cloud mass (Evans et al. 2014). These three clouds contain YSOs but there are no massive stars inside.

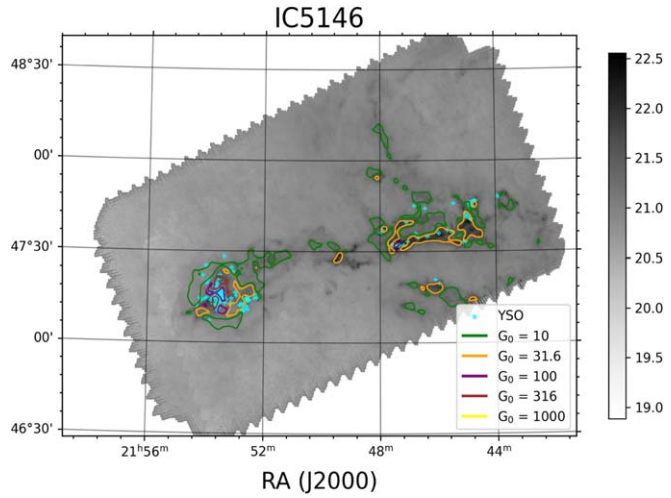

Figure A10. Contours of UV intensity overlaid on H_2 column density map of the IC 5146 region. The labels of the figure are the same as those in Figure 3.

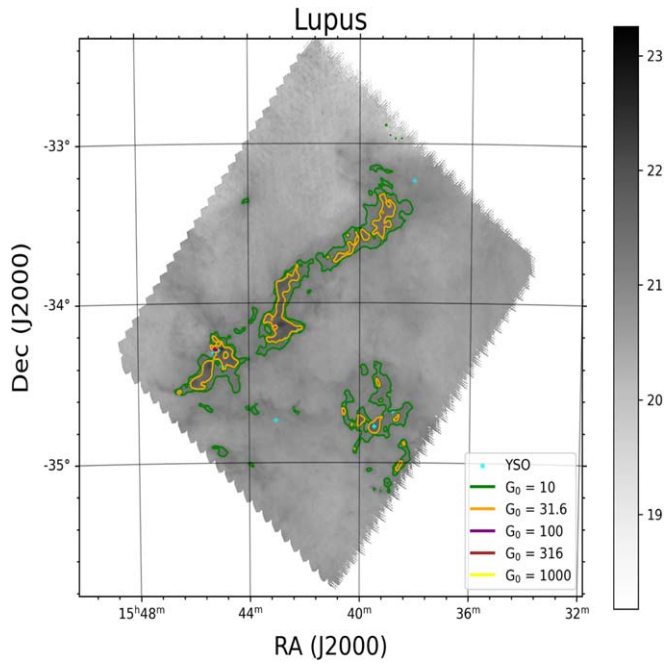

Figure A11. Contours of UV intensity overlaid on H_2 column density map of the Lupus I region. The labels in the figure are the same as those in Figure 3.

As shown in Figures A11, A12 and A13, the UV intensity distribution correlates with the existence of YSOs.

A.6. Musca

With distance of ∼200 pc, the Musca cloud is a 10.5 pc long filament with low-mass star formation (Cox et al. 2016). The mass of the Musca molecular cloud is about 335 $M_{\odot}$ (Evans et al. 2014).

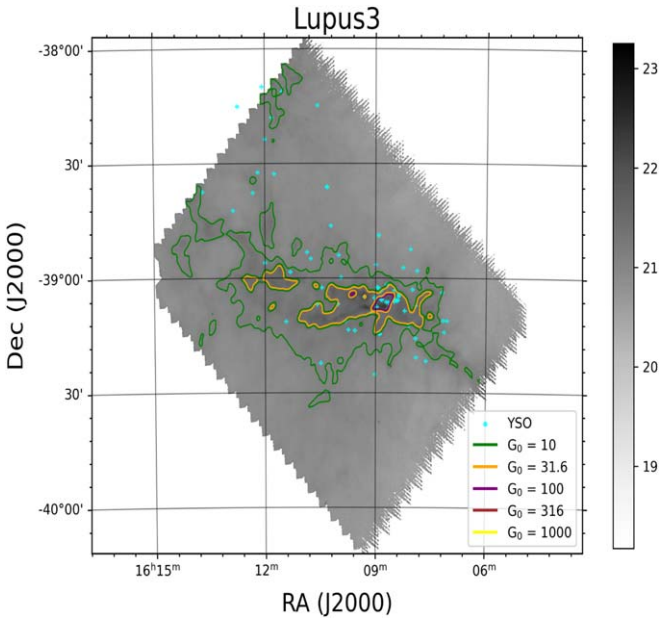

Figure A12. Contours of UV intensity overlaid on H_2 column density map of the Lupus III region. The labels in the figure are the same as those in Figure 3.

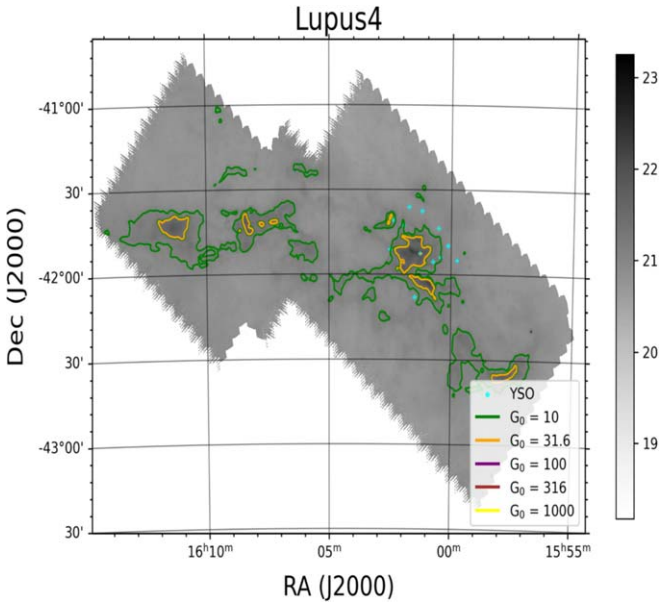

Figure A13. Contours of UV intensity overlaid on H_2 column density map of the Lupus IV region. The labels in the figure are the same as those in Figure 3.

There are no massive stars in this region. As is clear from Figure A14, UV intensity increases in some dense regions.

A.7. ρ Oph

With distance of 125 pc (Evans et al. 2014), the ρ Oph molecular cloud is one of the most conspicuous nearby regions where low and intermediate-mass star formation is taking place. The total mass of the ρ Oph cloud is about 3128 $M_{\odot}$, one third of which is dense gas. The ρ Oph cloud consists of two massive, centrally condensed cores, L1688 and L1689 (Loren 1989). Being different from L1689 with little star formation activity, L1688 harbors a rich cluster of YSOs at various evolutionary stages and is distinguished by high star formation efficiency (Wilking & Lada 1983). Two OB stars (HD 147 889 and ρ Oph A) are found in this region.

The UV radiation distribution of the ρ Oph cloud is depicted in Figure A15. A strong correlation between UV intensity and star distribution was found. The UV intensity G_0 can exceed 1000 in a dense gas region and regions around OB stars.

A.8. Perseus

The Perseus molecular cloud is ∼250 pc away with sky coverage of ∼10 deg^2. It is a low and intermediate-mass star-forming region. The total mass of the Perseus molecular cloud is about 6586 $M_{\odot}$, one third of which is dense gas (Evans et al. 2014). As demonstrated in Figure A16, the UV radiation field correlates with the locations of OB stars and YSOs in this region.

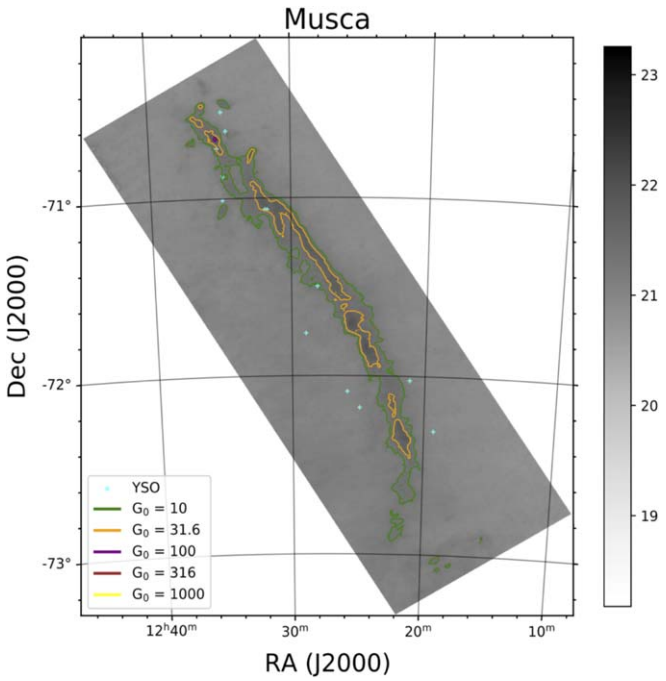

Figure A14. Contours of UV intensity overlaid on an H_2 column density map of the Musca region. The labels of the figure are the same as those in Figure 3.

A.9. Pipe

The Pipe Nebula has a distance of ∼145 pc (Alves & Franco 2007). Composed of an elongated dark cloud with length of 18 pc, the Pipe Nebula is one of the closest star-

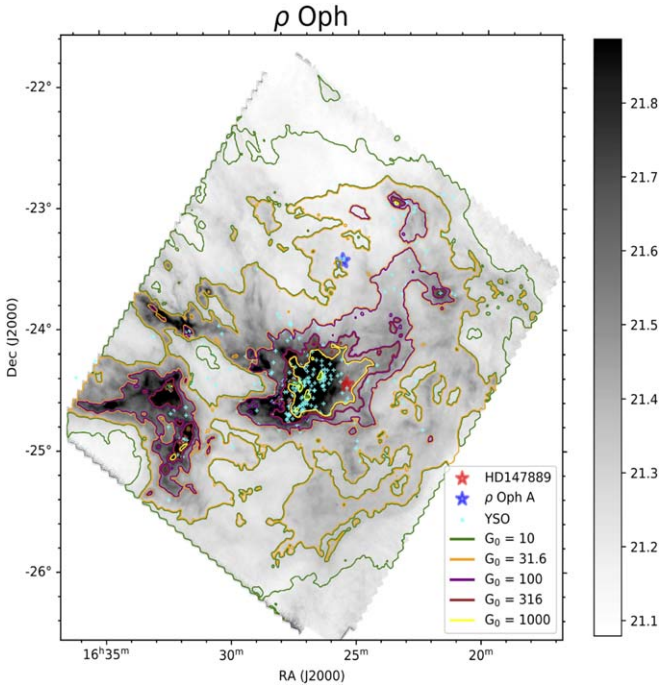

Figure A15. Contours of UV intensity overlaid on an H_2 column density map of the ρ Oph region. The labels in the figure are the same as those in Figure A2.

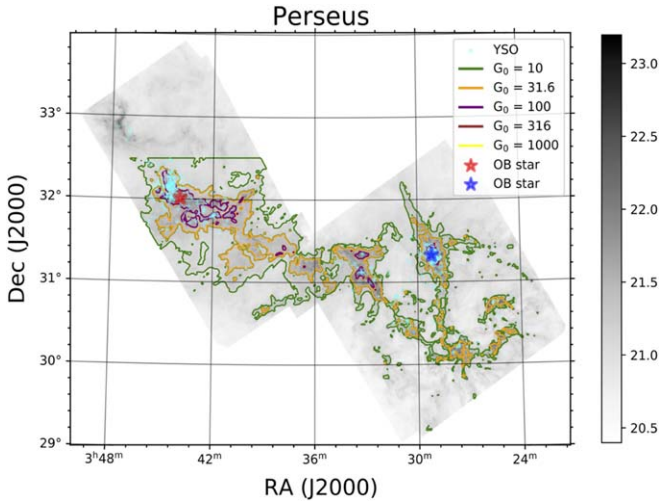

Figure A16. Contours of UV intensity overlaid on an H_2 column density map of the Perseus region. The labels in the figure are the same as those in Figure A2.

forming regions. The Pipe Nebula is an ideal target for investigating core formation. The mass of the Pipe Nebula is about 1.7×10^4 $M_\odot$ (Lombardi et al. 2006). A few identified YSOs were found in this region (Peretto et al. 2012). As affirmed in Figure A17, the UV intensity is very low ($G_0 <$ 31.6) toward most regions in this molecular complex.

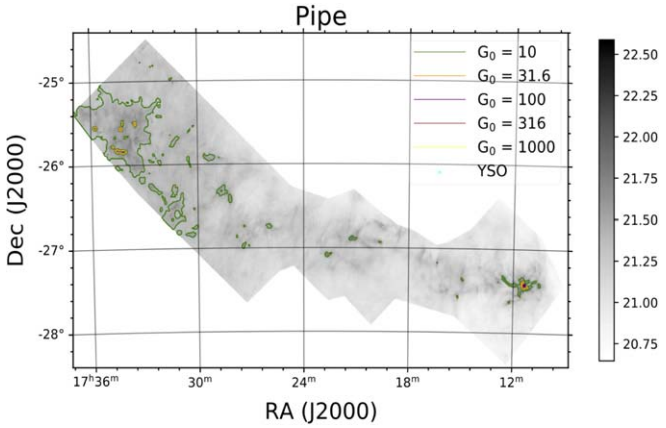

Figure A17. Contours of UV intensity overlaid on the H_2 column density map of the Pipe region. The labels in the figure are the same as those in Figure 3.

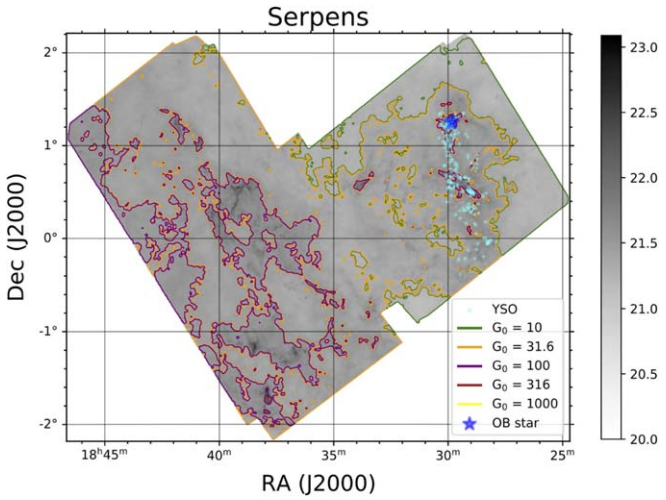

Figure A18. Contours of UV intensity overlaid on an H_2 column density map of the Serpens region. The labels in the figure are the same as those in Figure A2.

A.10. Serpens

The Serpens star-forming region located at ∼429 pc was covered ∼15 deg^2 by HGBS (Evans et al. 2014). Its total mass is ∼6583 $M_\odot$, two-thirds of which is dense gas (Evans et al. 2014). About 81% of the prestellar cores are found in the filamentary structure of Serpens (Fiorellino et al. 2021). Serpens is confirmed to be a low-mass and active star-forming region at a young age. As shown in Figure A18, lots of YSOs and an OB star are found in this region.

A.11. Taurus

The distance of the Taurus cloud to our solar system is about 140 pc (Palmeirim et al. 2013). The total mass of the Taurus

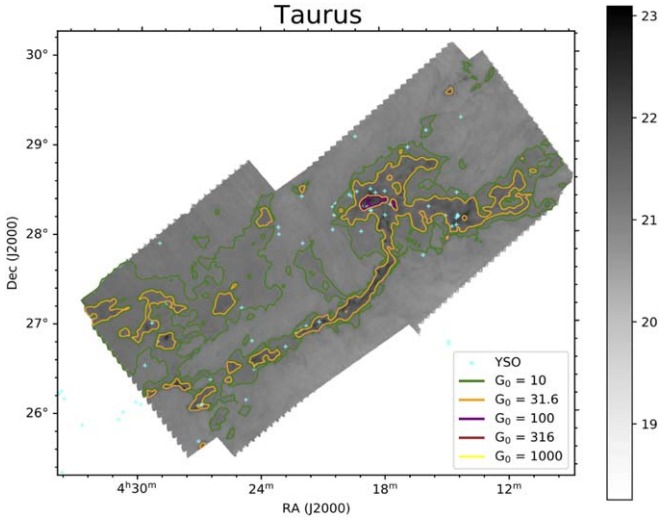

Figure A19. Contours of UV intensity overlaid on an H_2 column density map of the Taurus region. The labels in the figure are the same as those in Figure 3.

molecular cloud is about 2–4 $\times$ 10^4 $M_\odot$, ten percent of which is dense gas (Evans et al. 2014). HGBS covered about 52 deg^2 of this region (Kirk et al. 2013). No OB stars were found in the Taurus molecular cloud. As verified in Figure A19, the UV radiation intensity correlates with the distribution of dense gas.

ORCID iDs

Jifeng Xia (夏季风) https://orcid.org/0000-0003-3726-570X
Ningyu Tang https://orcid.org/0000-0002-2169-0472
Sihan Jiao https://orcid.org/0000-0002-9151-1388
Jinjin Xie https://orcid.org/0000-0002-2738-146X
Gary A. Fuller https://orcid.org/0000-0001-8509-1818
Di Li https://orcid.org/0000-0003-3010-7661

References

Alves de Oliveira, C., Schneider, N., Merín, B., et al. 2014, A&A, 568, A98
Alves, F. O., & Franco, G. A. P. 2007, A&A, 470, 597
André, P., Men'shchikov, A., Bontemps, S., et al. 2010, A&A, 518, L102
Arzoumanian, D., André, P., Könyves, V., et al. 2019, A&A, 621, A42
Bohlin, R. C., Savage, B. D., & Drake, J. F. 1978, ApJ, 224, 132
Bresnahan, D., Ward-Thompson, D., Kirk, J. M., et al. 2018, A&A, 615, A125
Cambrésy, L. 1999, A&A, 345, 965
Cox, N. L. J., Arzoumanian, D., André, P., et al. 2016, A&A, 590, A110
Di Francesco, J., Keown, J., Fallscheer, C., et al. 2020, ApJ, 904, 172
Dobashi, K., Bernard, J.-P., Yonekura, Y., & Fukui, Y. 1994, ApJS, 95, 419
Draine, B. T. 2011, Physics of the Interstellar and Intergalactic Medium (Princeton, NJ: Princeton Univ. Press)
Dunham, M. M., Arce, H. G., Allen, L. E., et al. 2013, AJ, 145, 94
Evans, N. J. I., Heiderman, A., & Vutisalchavakul, N. 2014, ApJ, 782, 114
Evans, N. J. I., Dunham, M. M., Jørgensen, J. K., et al. 2009, ApJS, 181, 321
Ferrière, K. M. 2001, Rev. Mod. Phys., 73, 1031
Fiorellino, E., Elia, D., André, P., et al. 2021, MNRAS, 500, 4257
Goldsmith, P. F. 2001, ApJ, 557, 736
Goldsmith, P. F., Heyer, M., Narayanan, G., et al. 2008, ApJ, 680, 428
Greenberg, J. M. 1968, in Nebulae and Interstellar Matter, ed. B. M. Middlehurst & L. H. Aller (Chicago, IL: Univ. Chicago Press), 221
Hao, C. N., Kennicutt, R. C. J., Johnson, B. D., et al. 2011, in ASP Conf. Series, 446, Galaxy Evolution: Infrared to Millimeter Wavelength Perspective (Guilin, China, 25–29 October 2010), ed. W. Wang et al. (San Francisco, CA: ASP), 63
Hara, A., Tachihara, K., Mizuno, A., et al. 1999, PASJ, 51, 895
Heithausen, A., & Thaddeus, P. 1990, ApJL, 353, L49
Hildebrand, R. H. 1983, QJRAS, 24, 267
Hughes, T. M., Ibar, E., Villanueva, V., et al. 2017, A&A, 602, A49
Ivezic, Z., & Elitzur, M. 1997, MNRAS, 287, 799
Kawamura, A., Onishi, T., Mizuno, A., Ogawa, H., & Fukui, Y. 1999, PASJ, 51, 851
Kennicutt, R. C. J. 1998, ARA&A, 36, 189
Kennicutt, R. C., & Evans, N. J. 2012, ARA&A, 50, 531
Kirk, J. M., Ward-Thompson, D., Palmeirim, P., et al. 2013, MNRAS, 432, 1424
Könyves, V., André, P., Arzoumanian, D., et al. 2020, A&A, 635, A34
Kroupa, P. 2002, Sci, 295, 82
Lada, C. J., Lombardi, M., & Alves, J. F. 2010, ApJ, 724, 687
Lada, E. A., Bally, J., & Stark, A. A. 1991, ApJ, 368, 432
Li, D., Goldsmith, P. F., & Menten, K. 2003, ApJ, 587, 262
Li, D., Goldsmith, P. F., & Xie, T. 1999, ApJ, 522, 897
Li, D., Kauffmann, J., Zhang, Q., & Chen, W. 2013, ApJL, 768, L5
Li, H., Li, D., Qian, L., et al. 2015, ApJS, 219, 20
Liseau, R., White, G. J., Larsson, B., et al. 1999, A&A, 344, 342
Liu, H. B. 2019, ApJL, 877, L22
Lombardi, M., Alves, J., & Lada, C. J. 2006, A&A, 454, 781
Loren, R. B. 1989, ApJ, 338, 902
Martin, D. C., Fanson, J., Schiminovich, D., et al. 2005, ApJL, 619, L1
Megeath, S. T., Gutermuth, R., Muzerolle, J., et al. 2012, AJ, 144, 192
Mizuno, A., Yamaguchi, R., Tachihara, K., et al. 2001, PASJ, 53, 1071
Nenkova, M., Ivezić, Ž, & Elitzur, M. 2000, in ASP Conf. Ser., 196, Thermal Emission Spectroscopy and Analysis of Dust, Disks, and Regoliths, 196, ed. M. L. Sitko, A. L. Sprague, & D. K. Lynch (San Francisco, CA: ASP), 77
Onishi, T., Kawamura, A., Abe, R., et al. 1999, PASJ, 51, 871
Palmeirim, P., André, P., Kirk, J., et al. 2013, A&A, 550, A38
Peretto, N., André, P., Könyves, V., et al. 2012, A&A, 541, A63
Pezzuto, S., Elia, D., Schisano, E., et al. 2012, A&A, 547, A54
Pineda, J. L., Velusamy, T., Langer, W. D., et al. 2010, A&A, 521, L19
Rachford, B. L., Snow, T. P., Destree, J. D., et al. 2009, ApJS, 180, 125
Robitaille, T., & Bressert, E. 2012, APLpy: Astronomical Plotting Library in Python, Astrophysics Source Code Library, ascl:1208.017
Roy, A., André, P., Palmeirim, P., et al. 2014, A&A, 562, A138
Rygl, K. L. J., Benedettini, M., Schisano, E., et al. 2013, A&A, 549, L1
Tatematsu, K., Umemoto, T., Heyer, M. H., et al. 1998, ApJS, 118, 517
Tielens, A. G. G. M., & Hollenbach, D. 1985, ApJ, 291, 722
Wang, S., Ren, Z., Li, D., et al. 2020, MNRAS, 499, 4432
Ward-Thompson, D., Di Francesco, J., Hatchell, J., et al. 2007, PASP, 119, 855
Wilking, B. A., & Lada, C. J. 1983, ApJ, 274, 698
Winston, E., Cox, N. L. J., Prusti, T., et al. 2012, A&A, 545, A145
Xie, J., Fuller, G. A., Li, D., et al. 2021, SCPMA, 64, 279511
Zucker, C., Speagle, J. S., Schlafly, E. F., et al. 2019, ApJ, 879, 125